

Swept-Angle Synthetic Wavelength Interferometry

Alankar Kotwal¹, Anat Levin², and Ioannis Gkioulekas¹
¹Carnegie Mellon University, ²Technion

Abstract

We present a new imaging technique, swept-angle synthetic wavelength interferometry, for full-field micron-scale 3D sensing. As in conventional synthetic wavelength interferometry, our technique uses light consisting of two narrowly-separated optical wavelengths, resulting in per-pixel interferometric measurements whose phase encodes scene depth. Our technique additionally uses a new type of light source that, by emulating spatially-incoherent illumination, makes interferometric measurements insensitive to aberrations and (sub)surface scattering, effects that corrupt phase measurements. The resulting technique combines the robustness to such corruptions of scanning interferometric setups, with the speed of full-field interferometric setups. Overall, our technique can recover full-frame depth at a lateral and axial resolution of $5\ \mu\text{m}$, at frame rates of 5 Hz, even under strong ambient light. We build an experimental prototype, and use it to demonstrate these capabilities by scanning a variety of objects, including objects representative of applications in inspection and fabrication, and objects that contain challenging light scattering effects.

1. Introduction

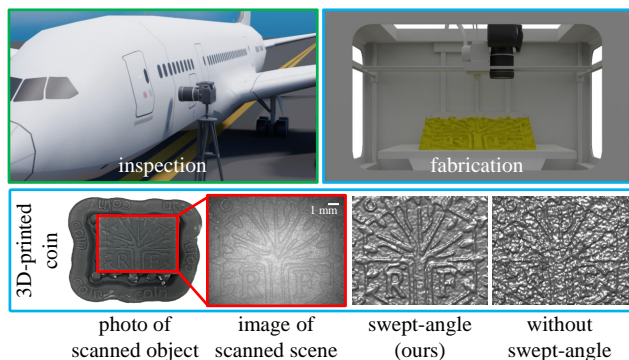


Figure 1. **Applications of swept-angle SWI in industrial inspection and fabrication.** We show depth reconstruction for a scene representative of the critical applications of SWI: a coin pattern 3D-printed by a commercial printer on a translucent material.

Depth sensing is among core problems of computer vision and computational imaging, with widespread applications in medicine, industry, and robotics. An array of

techniques is available for acquiring depth maps of three-dimensional (3D) scenes at different scales. In particular, micrometer-resolution depth sensing, our focus in this paper, is important in biomedical imaging because biological features are often micron-scale, industrial fabrication and inspection of critical parts that must conform to their specifications (Figure 1), and robotics to handle fine objects.

Active illumination depth sensing techniques such as lidar, structured light, and correlation time-of-flight (ToF) cannot provide micrometer axial resolution. Instead, we focus on *interferometric* techniques that can achieve such resolutions. The operational principles and characteristics of interferometric techniques vary, depending on the type of active illumination and optical configurations they use.

The choice of illumination spectrum leads to techniques such as optical coherence tomography (OCT), which uses broadband illumination, and phase-shifting interferometry (PSI), which uses monochromatic illumination. We consider synthetic wavelength interferometry (SWI), which operates between these two extremes: By using illumination consisting of two narrowly-separated optical wavelengths, SWI provides a controllable trade-off between the large unambiguous depth range of OCT, and the large axial resolution of PSI. SWI can achieve micrometer resolution at depth ranges in the order of hundreds of micrometers.

The choice of optical configuration results in full-field versus scanning implementations, which offer different trade-offs. Full-field implementations acquire entire 2D depth maps, offering simultaneously fast operation and pixel-level lateral resolutions. However, full-field implementations are very sensitive to effects that corrupt depth estimation, such as imperfections in free-space optics (e.g., lens aberrations) and indirect illumination (e.g., subsurface scattering). By contrast, scanning implementations use beam steering to sequentially scan points in a scene and produce a 2D depth map. Scanning implementations offer robustness to depth corruption effects, through the use of fiber optics to reduce aberrations, and co-axial illumination and sensing to eliminate most indirect illumination. However, scanning makes acquiring depth maps with pixel-level lateral resolution and megapixel sizes impractically slow.

We develop a 3D sensing technique, *swept-angle syn-*

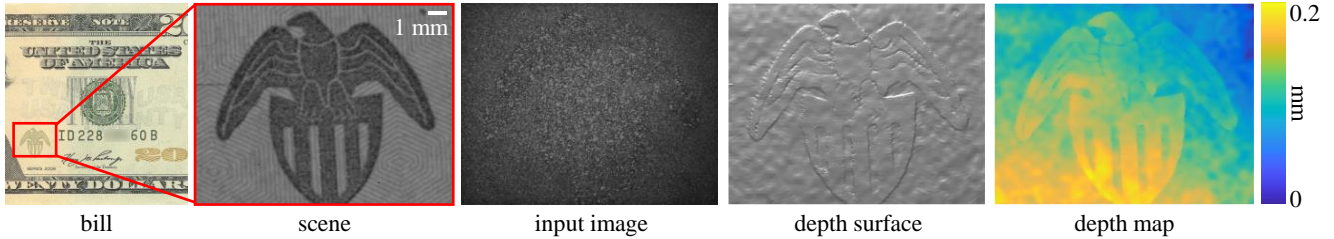


Figure 2. **Reconstructing the eagle embossed on a \$20 bill.** The features on the eagle are raised $10\ \mu\text{m}$ off the surface of the bill. The recovered depth shows fine details such as the gaps between the wings reconstructed with high lateral and axial resolution.

thetic wavelength interferometry, that combines the complementary advantages of full-field and scanning implementations. We draw inspiration from previous work showing that the use of *spatially-incoherent illumination* in full-field interferometry mitigates aberration and indirect illumination effects. We design a light source that emulates spatial incoherence, by scanning *within exposure* a dichromatic point source at the focal plane of the illumination lens, effectively sweeping the illumination angle—hence *swept-angle*. We combine this light source with full-field SWI, resulting in a 3D sensing technique with the following performance characteristics: 5 Hz full-frame 2 Mpixel acquisition; $5\ \mu\text{m}$ lateral and axial resolution; range and resolution tunability; and robustness to aberrations, ambient illumination, and indirect illumination. We build an experimental prototype, and use it to demonstrate these capabilities, as in Figure 2. We provide setup details, reconstruction code, and representative data in the supplement, and will release all our data upon acceptance.

Potential impact. Swept-angle SWI can be useful and relevant for critical applications, including industrial fabrication and inspection. In industrial fabrication, swept-angle SWI can be used to provide feedback during additive and subtractive manufacturing processes [67]. In industrial inspection, swept-angle SWI can be used to examine newly-fabricated or used in-place critical parts and ensure they comply with operational specifications. Swept-angle SWI, uniquely among 3D scanning techniques, offers a combination of operational characteristics that are critical for both applications: First, high acquisition speed, which is necessary to avoid slowing down the manufacturing process, and to perform inspection efficiently. Second, micrometer lateral and axial resolution, which is necessary to detect critical defects. Third, robustness to aberrations and indirect illumination, which is necessary because of the materials used for fabrication, which often have strong subsurface scattering. Figure 1 showcases a result representative of these applications: We use swept-angle SWI to scan a coin pattern 3D-printed by a commercial material printer on a translucent material at axial and lateral scales of a couple dozen micrometers.

Table 1. Comparison of interferometric depth sensing techniques for millimeter-scale scenes. (‘f.f.’: full-field; ‘scan.’: scanning)

method	axial res	lateral res	depth range	acq time	robust
f.f. TD-OCT	✓	✓	✓	✗	✓
scan. FD-OCT	✗	✓	✓	✗	✓
scan. SS-OCT	✗	✓	✓	✗	✓
f.f. PSI	✓	✓	✗	✓	✗
scan. PSI	✗	✓	✗	✗	✓
f.f. SWI	✓	✓	✓	✓	✗
scan. SWI	✗	✓	✓	✗	✓
f.f. SA-SWI	✓	✓	✓	✓	✓

2. Related work

Depth sensing. Thanks to the central role of depth sensing in computer vision, there exists a large array of techniques for acquiring depth. Passive techniques rely on the appearance of the scene under external, ambient light, and use cues such as stereo [4, 30, 52], (de)focus [21, 31, 69], or shading [28, 34]. Active techniques inject controlled lighting into the scene, to overcome issues such as lack of texture and limited resolution. These include structured light [6, 24, 58, 65], impulse ToF [2, 19, 22, 23, 32, 39, 47, 54, 56, 64, 71, 72], and correlation ToF [3, 15, 16, 26, 27, 33, 43, 44, 60, 62, 66]. These techniques cannot easily achieve axial resolutions below hundreds of micrometers, placing them out of scope for applications requiring micrometer resolutions.

Optical interferometry. Interferometry is a classic wave-optics technique that measures the correlation, or *interference*, between two or more light beams that have traveled along different paths [29]. Most relevant to our work are three broad classes of interferometric techniques that provide depth sensing capabilities with different advantages and disadvantages, which we summarize in Table 1.

Phase-shifting interferometry (PSI) techniques [9, 37] use single-frequency illumination for nanometer-scale depth sensing. Similar to correlation ToF, they estimate depth by measuring the phase of a sinusoidal waveform. However, whereas correlation ToF uses external modulation to generate megahertz-frequency waveforms, PSI directly uses the terahertz-frequency light waveform. Unfortunately, the unambiguous depth range of PSI is limited to the illumination wavelength, typically around a micrometer.

Synthetic wavelength interferometry (SWI) (or *hetero-*

dyne interferometry) techniques [7, 8, 10, 14, 45, 46] use illumination comprising multiple narrow spectral bands to *synthesize* waveforms at frequencies between the megahertz rates of correlation ToF and terahertz rates of PSI. These techniques allow control of the trade off between unambiguous depth range and resolution, by tuning the frequency of the *synthetic wavelength*. As our technique builds upon SWI, we detail its operational principles in Section 3.

Lastly, *optical coherence tomography* (OCT) techniques [20, 35, 41] use broadband illumination to perform depth sensing analogously to impulse time-of-flight, by processing temporally-resolved (transient) responses. OCT decouples range and resolution, achieving unambiguous depth ranges up to centimeters, at micrometer axial resolutions. This flexibility comes at the cost of a steep increase in acquisition time, because of the need to perform axial (for time-domain OCT) or lateral (for Fourier-domain and swept-source OCT) scanning [13].

Mitigating indirect illumination effects. In their basic forms, active depth sensing techniques assume the presence of only direct illumination in the scene. *Indirect illumination* effects, such as interreflections and subsurface scattering, confound depth information. For example, in correlation ToF techniques (including PSI and SWI), indirect illumination results in incorrect phase, and thus depth estimation, an effect also known as *multi-path interference*. Several techniques exist for *computationally* mitigating indirect illumination effects, using models of multi-bounce transport [18, 36, 51], sparse reconstruction [17, 38], multi-wavelength approaches [5], and neural approaches [49, 68].

Other techniques focus on *optically* removing indirect illumination by *probing light transport* [59]. Probing techniques use spatial modulation of the illumination and camera, and include schemes such as epipolar imaging [55, 58], high-spatial-frequency illumination [53, 63], and spatio-temporal code illumination [1, 25, 57]. Similar probing capabilities can be implemented in interferometric systems, by exploiting the spatio-temporal coherence properties of the illumination [20, 41]. We adapt these techniques for use with SWI, to enable robust micrometer depth sensing.

3. Background on interferometry

The Michelson interferometer. Our optical setup is based on the classical Michelson interferometer (Figure 3(c)). The interferometer uses a beam splitter to divide collimated input illumination into two beams: one propagates toward the *scene arm*, and another propagates toward the *reference arm*—typically a planar mirror mounted on a translation stage that can vary the mirror’s distance from the beam splitter. After reflection, the two light beams recombine at the beam splitter and propagate toward the sensor.

We denote by l and $d(x)$ the distance from the beam-splitter of the reference mirror and the scene point that pixel x images, respectively. As l is a controllable parameter, we

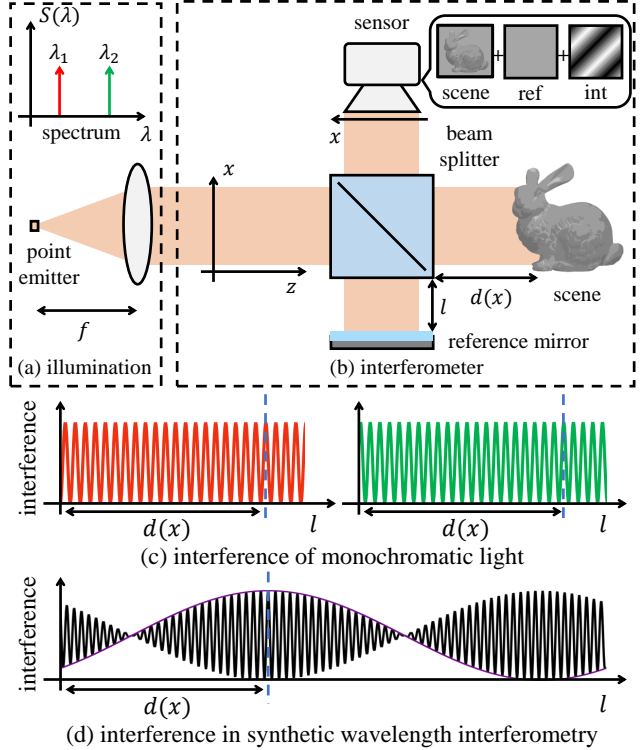


Figure 3. **Synthetic wavelength interferometry.** (a-b) Collimated illumination from a point source emitting at two narrowly-separated wavelengths is injected into a Michelson interferometer. (c) As the reference mirror position l is scanned, each wavelength contributes to the interference a sinusoid with period equal to its wavelength. (d) The sum of these sinusoids has an envelope that is another sinusoid at a *synthetic wavelength* peaked at $l = d(x)$.

denote it explicitly. We denote by $\mathbf{u}_r(x, l)$ and $\mathbf{u}_s(x)$ the complex fields arriving at sensor pixel x from the reference and scene arms respectively. Then, the sensor measures,

$$I(x, l) = \underbrace{\|\mathbf{u}_s(x)\|^2 + \|\mathbf{u}_r(x, l)\|^2}_{\equiv \mathcal{I}(x, l)} + 2 \operatorname{Re} \left\{ \underbrace{\mathbf{u}_s(x) \mathbf{u}_r^*(x, l)}_{\equiv \mathcal{C}(x, l)} \right\}. \quad (1)$$

The first two terms in Equation (1) correspond to the intensities the sensor would measure if it were observing each of the two arms separately. We call their sum the *interference-free* image \mathcal{I} . The third term, which we call *interference*, is the real part of the complex *correlation* \mathcal{C} between the reflected scene and reference fields. We elaborate on how to isolate the interference term from Equation (1) in Section 4.

Synthetic wavelength interferometry. SWI uses illumination comprising two distinct, but narrowly-separated, wavelengths that are incoherent with each other. We denote these wavelengths as λ and $\lambda/1+\epsilon$, corresponding to wavenumbers $\kappa \equiv 2\pi/\lambda$ and $(1+\epsilon)\kappa$, respectively. We assume that this illumination is injected into the interferometer as a collimated beam—for example, created by placing the outputs of two fiber-coupled single-frequency lasers at the focal plane of a lens, as in Figures 3 and 5. Then, we show in the supple-

ment that the correlation $\mathcal{C}(x, l)$ equals

$$\mathcal{C}(x, l) = \exp(-2i\kappa(d(x) - l)) [1 + \exp(-2i\kappa\epsilon(d(x) - l))]. \quad (2)$$

The interference component of the camera intensity measurements in Equation (1) equals,

$$\text{Re}(\mathcal{C}(x, l)) = 2 \sin(\kappa(2+\epsilon)(d(x) - l)) \sin(\kappa\epsilon(d(x) - l)) \quad (3)$$

$$\approx 2 \sin(2\kappa(d(x) - l)) \sin(\kappa\epsilon(d(x) - l)). \quad (4)$$

The approximation is accurate when $\epsilon \ll 1$, i.e., when the two wavelengths are close. We observe that, as a function of $d(x) - l$, the interference is the product of two sinusoids: first, a *carrier sinusoid* with *carrier wavelength* $\lambda_c \equiv \lambda/2$ and corresponding *carrier wavenumber* $\kappa_c \equiv 2\lambda$; second, an *envelope sinusoid* \mathcal{E} with *synthetic wavelength* $\lambda_s \equiv \lambda/\epsilon$ and corresponding *synthetic wavenumber* $\kappa_s \equiv \epsilon\kappa$:

$$\mathcal{E}(x, l) \equiv \sin(\kappa\epsilon(d(x) - l)). \quad (5)$$

Figure 3(d) visualizes $\text{Re}\{\mathcal{C}(x, l)\}$ and $\mathcal{E}(x, l)$.

From Equation (5), we see that SWI encodes scene depth $d(x)$ in the phase $\phi(d(x)) \equiv \kappa\epsilon(d(x) - l)$ of the envelope sinusoid. We defer details on how to measure the envelope and estimate this phase until Section 4. We make two observations: First, SWI provides depth measurements at intervals of $[0, \lambda_s]$, and cannot disambiguate between depths differing by an integer multiple of λ_s . Second, the use of two wavelengths makes it possible to control the unambiguous depth range: By decreasing the separation ϵ between the two emitted wavelengths, we increase the unambiguous depth range, at the cost of decreasing depth resolution.

Full-field and scanning interferometry. Figure 5 shows two types of Michelson interferometer setups that implement SWI: (a) a full-field interferometer; and (b) a scanning interferometer. We discuss their relative merits, which will motivate our proposed swept-angle interferometer setup.

Full-field interferometers (Figure 5(a)) use *free-space optics* (lenses, beamsplitters) to illuminate and image the entire field of view in the scene and reference arms. They also use a two-dimensional sensor to measure interference at all locations x . This enables fast interference measurements for all scene points at once, and at lateral resolutions as high as the pixel pitch of the sensor.

Unfortunately, full-field interferometers are susceptible to phase corruption effects, as we visualize in Figure 4. Equation (5) assumes that the scene field is due to only the *direct* light path (solid line in Figure 4(a)), which produces a sinusoidal envelope with phase delay $d(x)$ (solid orange curve in Figure 4(b)). In practice, the scene field will include contributions from additional paths: First, *indirect* paths due to subsurface scattering (dashed lines in Figure 4(a)). Second, stray paths due to optical aberrations (Figure 4(c)). These paths have different lengths, and thus contribute to the envelope sinusoidal terms of different phases (dashed curves in Figure 4(b)). Their summation

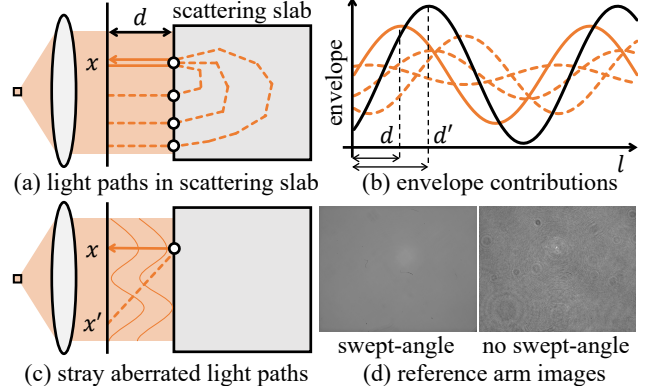


Figure 4. **Phase corruption effects.** (a) A typical scene contains both direct (solid line) and indirect (dashed lines) light paths. (b) The direct path contributes a sinusoid with the correct phase (solid orange line). The indirect paths contribute sinusoids with incorrect phases (dashed lines). Their summation results in erroneous phase estimation (dark solid line). (c) Aberrations in free-space optics result in stray light paths that also contribute incorrect phases. (d) Images of the reference arm (mirror) visualize the effects of aberrations, and their mitigation using swept-angle illumination.

produces an overall sinusoidal envelope (black) with phase $d' \neq d(x)$, resulting in incorrect depth estimation.

Scanning interferometers (Figure 5(b)) use *fiber optics* (couplers, circulators, collimators) to generate a focused beam that illuminates only one point in the scene and reference arms. Additionally, they use a single-pixel sensor, focused at the same point. They also use steering optics (e.g., MEMS mirrors) to scan the focus point and capture interference measurements for the entire scene.

Scanning interferometers effectively mitigate the phase corruption effects in Figure 4: Because, at any given time, they only illuminate and image one point in the scene, they eliminate contributions from indirect paths such as those in Figure 4(a). Additionally, because the use of fiber optics minimizes aberrations, they eliminate stray paths such as those in Figure 4(c). Unfortunately, this robustness comes at the cost of having to use beam steering to scan the entire scene. This translates into long acquisition times, especially when it is necessary to measure depth at pixel-level lateral resolutions and at a sensor-equivalent field of view.

In the next section, we introduce an interferometer design that combines the fast acquisition and high lateral resolution of full-field interferometers, with the robustness to phase corruption effects of scanning interferometers.

4. Swept-angle illumination

In this section, we design a new light source for use with full-field SWI, to mitigate the phase corruption effects shown in Figure 4—indirect illumination, aberrations. Figure 5(c) shows our final *swept-angle* optical design.

Interferometry with spatially-incoherent illumination. Our starting point is previous findings on the use of *spatially-incoherent illumination* in full-field interferomet-

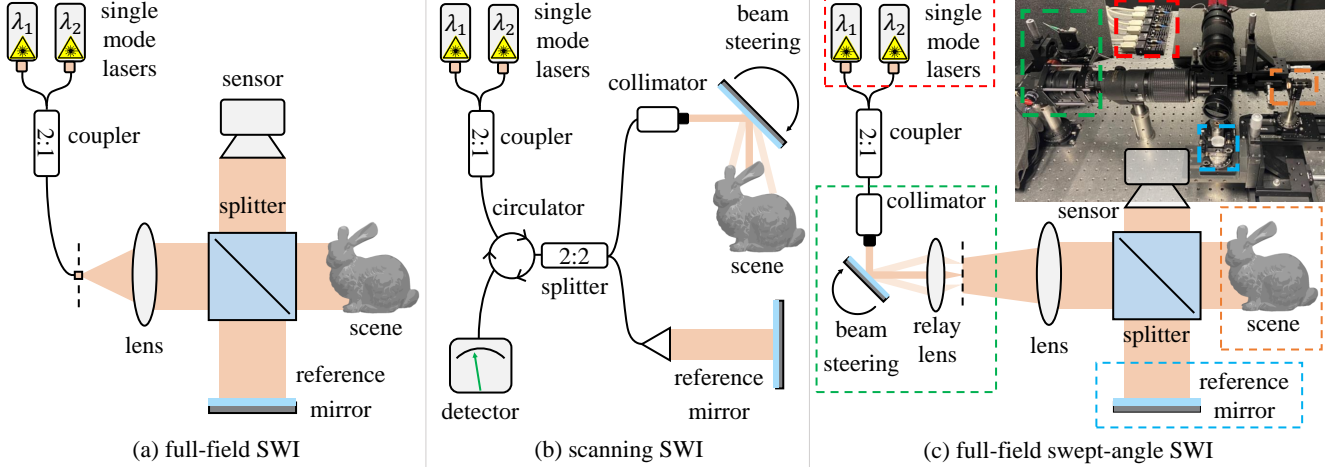


Figure 5. **Synthetic wavelength interferometry setups.** (a) A full-field interferometer efficiently acquires full-frame depth, but is susceptible to phase corruptions due to aberrations and indirect illumination. (b) A scanning interferometer is robust to such corruptions, but requires slow lateral scanning. (c) A swept-angle full-field interferometer achieves both efficiency and robustness.

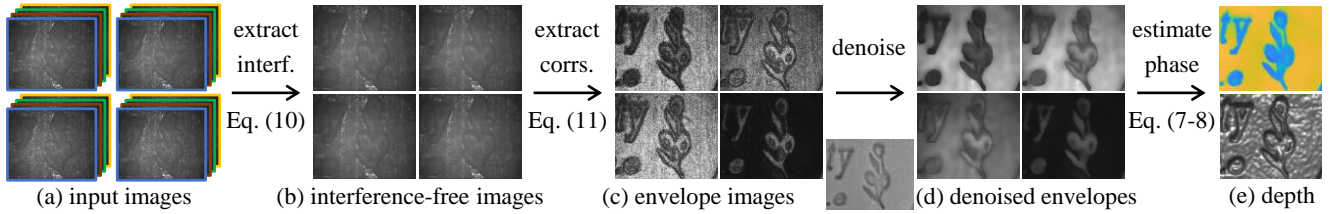


Figure 6. **The $\{4, 4\}$ phase retrieval pipeline.** (a) We take intensity measurements at 16 reference positions, corresponding to 4 synthetic by 4 carrier subwavelength shifts. (b) and (c) For each synthetic sub-wavelength shift, we estimate *interference-free* and *envelope* images. (d) We denoise the envelope image using joint bilateral filtering. (e) We use 4-shift phase retrieval to estimate envelope phase and depth.

ric implementations. Specifically, Gkioulekas et al. [20] showed that using spatially incoherent illumination in a Michelson interferometer is equivalent to *direct-only probing*: this optically rejects indirect paths and makes the correlation term \mathcal{C} depend predominantly on contributions from direct paths. Additionally, Xiao et al. [73] showed that using spatially-incoherent illumination makes the correlation term \mathcal{C} insensitive to aberrations in the free-space optics.

Both Gkioulekas et al. [20] and Xiao et al. [73] realize spatially-incoherent illumination by replacing the point emitter in Figure 3 with an area emitter, e.g., LED or halogen lamp. Unfortunately, fundamental physics dictate that extending emission area of a light source is coupled with broadening its emission spectrum. This coupling was not an issue for prior work, which focused on OCT applications that require broadband illumination; but it makes spatially-incoherent light sources incompatible with SWI, which requires narrow-linewidth dichromatic illumination.

Emulating spatial coherence. To resolve this conundrum, we consider the following: Replacing the point emitter in Figure 3 with an area emitter changes the illumination, from a single collimated beam parallel to the optical axis, to the superposition of beams traveling along directions offset from the optical axis by angles $\theta \in [-\Theta/2, \Theta/2]$, where Θ depends on the emission area and lens focal length. We

denote by $\mathbf{u}_s^\theta(x)$ and $\mathbf{u}_r^\theta(x, l)$ the complex fields resulting by each such beam reflecting on the scene and reference arms. Then, because different points on the area emitter are incoherent with each other, we can update Equation (1) as

$$I(x, l) = \int_{\theta} I^\theta(x, l) d\theta,$$

$$\mathcal{I}(x, l) = \int_{\theta} \mathcal{I}^\theta(x, l) d\theta, \quad \mathcal{C}(x, l) = \int_{\theta} \mathcal{C}^\theta(x, l) d\theta, \quad (6)$$

$$I^\theta(x, l) \equiv \underbrace{\|\mathbf{u}_s^\theta(x)\|^2 + \|\mathbf{u}_r^\theta(x, l)\|^2}_{\equiv \mathcal{I}^\theta(x, l)} + 2 \operatorname{Re}\{\underbrace{\mathbf{u}_s^\theta(x)\mathbf{u}_r^{*\theta}(x, l)}_{\equiv \mathcal{C}^\theta(x, l)}\}.$$

We can interpret Equation (6) as follows: the image I measured using an area emitter equals the sum of the images that would be measured using independent point emitters spanning the emission area, each producing illumination at an angle θ (and respectively for correlation \mathcal{C}).

With this interpretation at hand, we design the setup of Figure 5(c) to emulate a spatially-incoherent source suitable for SWI through time-division multiplexing: We use a galvo mirror to steer a narrow collimated beam of narrow-linewidth dichromatic illumination. We focus this beam through a relay lens at a point on the focal plane of the illumination lens. As we steer the beam direction, the focus point scans an area on this focal plane. In turn, each point

location results in the injection of illumination at an angle θ in the interferometer. By performing a full scan of the focus point over a target effective emission area *within a single exposure*, the acquired image and correlation measurements will equal those of Equation (6). As this design sweeps the illumination angle within exposure, we term it *swept-angle illumination*, and its combination with full-field SWI *swept-angle synthetic wavelength interferometry*.

Comparison to Kotwal et al. [41]. The illumination module of the proposed setup in Figure 5(c) is an adaptation of the Fourier-domain redistributive projector of Kotwal et al. [41]. Compared to their setup, we do not need to use an amplitude electro-optic modulator, as we are only interested in emulating spatial incoherence (equivalent, direct-only probing). Additionally, their setup was designed for use with monochromatic illumination, to enable different light transport probing capabilities. By contrast, we use our setup with narrow-linewidth dichromatic illumination, to enable synthetic wavelength interferometry. More broadly, our key insight is that swept-angle illumination can emulate extended-area emitters with arbitrary spectral profiles.

5. The $\{M, N\}$ -shift phase retrieval algorithm

We now discuss our pipeline for acquiring and processing image measurements to estimate the envelope phase, and thus depth. For this, in the setup of Figure 5(c), we will use a nanometer-accuracy translation stage to vary the location l of the reference mirror.

Phase retrieval. We estimate the envelope phase using the classical N -shift phase retrieval algorithm [9, 42]: We assume we have estimates of the envelope $\mathcal{E}(x, l_n)$ at reference locations l_n corresponding to shifts by N -th fractions of the *synthetic* wavelength λ_s , $l_n = l + n\lambda_s/N$, $n \in \{0, \dots, N-1\}$. Then, we estimate the envelope phase as

$$\phi(d(x)) = \arctan \left[\frac{\sum_{n=0}^{N-1} \mathcal{E}(x, l_n) \sin(2\pi n/N)}{\sum_{n=0}^{N-1} \mathcal{E}(x, l_n) \cos(2\pi n/N)} \right], \quad (7)$$

and the depth (up to an integer multiple of λ_s) as

$$d(x) = l + \phi(d(x))/\kappa_s. \quad (8)$$

Envelope estimation. Equation (7) requires estimates of the envelope $\mathcal{E}(x, l_n)$ at each location l_n . To estimate these values, for each l_n , we capture intensity measurements $I(x, l_n^m)$ at M reference locations corresponding to shifts by M -th fractions of the *carrier* wavelength, $l_n^m = l_n + m\lambda_c/M$, $m \in \{0, \dots, M-1\}$. As the carrier wavelength λ_c is half the optical wavelength λ and orders of magnitude smaller than the synthetic wavelength λ_s , the envelope and interference-free image remain approximately constant across these shifts, $\mathcal{E}(x, l_n^m) \approx \mathcal{E}(x, l_n)$, $\mathcal{I}(x, l_n^m) \approx \mathcal{I}(x, l_n)$. Then, from Equations (1) and (4),

$$I(x, l_n^m) = \mathcal{I}(x, l_n) + 2 \sin(\kappa_c(d(x) - l_n^m)) \mathcal{E}(x, l_n). \quad (9)$$

We estimate the interference-free image and envelope as

$$\mathcal{I}(x, l_n) = 1/M \sum_{m=0}^{M-1} I(x, l_n^m), \quad (10)$$

$$|\mathcal{E}(x, l_n)| = \sqrt{1/2M \sum_{m=0}^{M-1} (I(x, l_n^m) - \mathcal{I}(x, l_n))^2}. \quad (11)$$

Equation (11) estimates envelope only up to sign. In the supplement we show that the missing sign does not matter when we use these estimates with Equation (7).

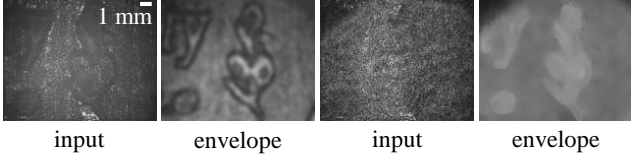
Equations (10), (11), (7), and (8) conclude our phase estimation pipeline, which we summarize in Figure 6. We provide more algorithmic details and pseudocode in the supplement. We call this pipeline the $\{M, N\}$ -shift phase retrieval algorithm. The parameters M and N are design parameters that we can fine-tune to control a trade-off between acquisition time and depth accuracy: As we increase M and N , the number $M \cdot N$ of total images we need to capture also increases; at the same time, the final depth estimate becomes more robust to noise. The theoretical minimum number of images is achieved using $\{3, 3\}$ shifts, corresponding to 9 images. In practice, we found that $\{4, 4\}$ shifts perform robustly across all scenes we scanned. We evaluate different $\{M, N\}$ combinations in the supplement.

Dealing with speckle. Interference in non-specular scenes takes the form of *speckle*, a high-frequency pseudo-random pattern (Figure 6(a)). This can result in very noisy envelope, and thus phase and depth, estimates. As we show in Figure 4(d), our use of swept-angle illumination greatly mitigates the effects of speckle. We can further reduce the impact of speckle by denoising the estimated quantities with a low-pass filter (e.g., Gaussian), as in prior work [20, 41]. Alternatively, to avoid blurring image details, we can use joint bilateral filtering [12, 61] with a guide image of the scanned scene captured under ambient light. Empirically, we found it advantageous to blur the envelope estimates of Equation (11) before using them in Equation (7) (Figure 6(d)), compared to blurring the phase or depth estimates.

6. Experiments

Experimental prototype. For all our experiments, we use the experimental prototype in Figure 5(c). Our prototype comprises: two distributed-Bragg-reflector lasers (wavelengths 780 nm and 781 nm, power 45 mW, linewidth 1 MHz); a galvo mirror pair; a translation stage (resolution 10 nm); two compound macro lenses (focal length 200 mm); a CCD sensor (pixel pitch 3.7 μm , 3400 \times 2700 pixels); and other free-space optics and mounts. We provide a detailed component list and specifications, calibration instructions, and other information about the setup in the supplement.

We use the following experimental specifications: The reproduction ratio is 1:1, the field of view is 12.5 mm \times 10 mm, and the working distance is 400 mm. The unambiguous depth range is approximately 500 μm . We use $\{4, 4\}$ -shifts (16 images), and a minimum per-image expo-



(a) with swept-angle source (b) without swept-angle source

Figure 7. **Effect of swept-angle scanning.** Swept-angle illumination helps mitigate speckle noise and subsurface scattering effects.

sure time of 10 ms, resulting at a frame rate of 5 Hz.

Depth recovery on challenging scenes. In Figures 8 and 2, we show scans of a variety of challenging scenes. We scan materials ranging from rough metallic (coins), to diffuse (music box, pill), to highly-scattering (soap and chocolate). Most of our scenes include fine features requiring high lateral and axial resolution (music box, business card, US quarter, dollar bill). We compare scan results using swept-angle SWI (with bilateral or Gaussian filtering), versus conventional full-field SWI (Figure 5(a), emulated by deactivating the angle-sweep galvo). In all scenes, the use of swept-angle illumination greatly improves reconstruction quality. The difference is more pronounced in scenes with strong subsurface scattering (music box, chocolate, soap). Even in metallic scenes where there is no subsurface scattering (coins), the use of swept-angle illumination still improves reconstruction quality, by helping mitigate aberration artifacts. Between bilateral versus Gaussian filtering, bilateral filtering helps preserve higher lateral detail.

Comparison with upsampled scanning SWI. A direct comparison of swept-angle SWI with scanning SWI is challenging, because of the differences between scanning and full-field setups (Figure 5, (b) versus (a), (c)). To qualitatively assess their relative performance, in Figure 9 we use the following experimental protocol: We downsample the depth map from our technique, by a factor of 35 in each dimension. This is approximately equal to the number of depths points a scanning SWI system would acquire at the same total exposure time as ours, when equipped with beam-steering optics that operate at a 30 kHz scan rate—we detail the exact calculation in the supplement. We then use joint bilateral upsampling [40] with the same guide image as in our technique, to upsample the downsampled depth map back to its original resolution. We observe that, due to the sparse set of points scanning SWI can acquire within the exposure time, the reconstructions miss fine features such as the hair on the quarter and letters on the business card.

Axial resolution. To quantify the axial resolution of our technique, we perform the following experiment. We use a second nanometer-accurate translation stage to place the chocolate scene from Figure 8 at different depths from the camera, at increments of $1\ \mu\text{m}$. We choose this scene because it is characterized by strong sub-surface scattering. We then compare how well full-field SWI with and without swept-angle illumination can track the scene depth. We per-

Table 2. **Depth accuracy.** MedAE is the median absolute error between ground truth and estimated depth. Kernel width is the lateral size of the speckle blur filter. All quantities are in μm .

kernel width	with swept-angle		w/o swept-angle	
	RMSE	MedAE	RMSE	MedAE
7	8.2	4.8	18.9	13.2
15	5.1	3.6	11.2	9.5
21	2.0	1.6	10.5	7.3
30	1.6	1.0	11.1	6.7

form this experiment using Gaussian filtering with kernels of different sizes, to additionally quantify lateral resolution. The results in Table 2 show that we can achieve an axial resolution of approximately $5\ \mu\text{m}$ and $1\ \mu\text{m}$, for kernel sizes $7\ \mu\text{m}$ and $30\ \mu\text{m}$, respectively. We can trade off lateral for axial resolution, by increasing filtering kernel size during phase retrieval. Figure 8 shows that this trade-off can become more favorable using bilateral filtering.

Additional experiments. In the supplement, we show many additional experiments, including: 1) *Comparisons with full-field OCT.* We show that swept-angle SWI can approximate the reconstruction quality of OCT, despite being $50\times$ faster. 2) *Tunable depth range.* We show that, by adjusting the wavelength separation between the two lasers, swept-angle SWI can scan macroscopic scenes with depth range 16 mm at resolution $50\ \mu\text{m}$, at significantly better quality than conventional full-field SWI. 3) *Robustness to ambient lighting.* We show that the use of near-monochromatic illumination makes swept-angle SWI robust to strong ambient lighting, even at 10% signal-to-background ratios. 4) *Effect of $\{M, N\}$ settings.* We show that, by adjusting the $\{M, N\}$ parameters of our phase retrieval algorithm, swept-angle SWI can trade-off between acquisition time versus reconstruction quality.

7. Limitations and conclusion

Phase wrapping As discussed in Section 3, because SWI computes depth from phase, it only determines depth up to an integer multiple of the synthetic wavelength λ_s . Equivalently, all depths in the scene are *wrapped* to $[0, \lambda_s]$, even if the depth range is greater. To mitigate phase wrapping and extend the unambiguous depth range, it is common to capture measurements at multiple synthetic wavelengths, and use them to *unwrap* the phase estimate [3, 7, 8, 11]. Whereas, theoretically, two synthetic wavelengths are enough to uniquely determine all depths, in practice phase unwrapping techniques are very sensitive to measurement noise [25]. Combining phase unwrapping algorithms with our technique is an interesting future direction.

Toward real-time operation The prototype in Figure 5(a) acquires measurements at a frame rate of 5 Hz, due to the need for 10 ms per-frame exposure time. If we use a stronger laser to reduce this time, the main bottleneck towards faster operation will be the need to perform phase shifts by physically translating the reference mirror. We can

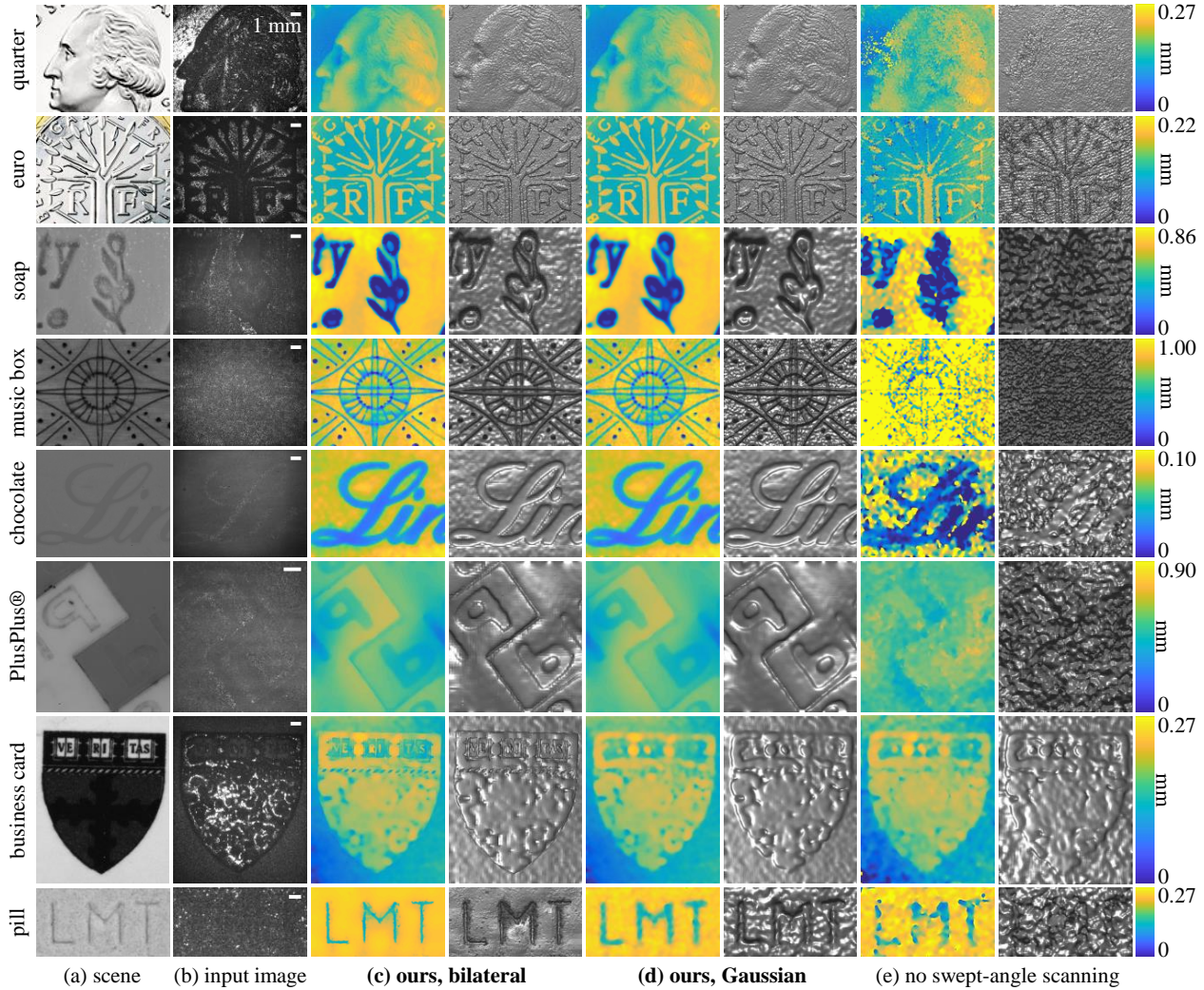


Figure 8. **Depth reconstruction.** Depth maps (left) and surface renderings (right) acquired using full-field SWI with: (c) swept-angle scanning and bilateral filtering; (d) swept-angle scanning and Gaussian filtering; (e) no swept-angle scanning

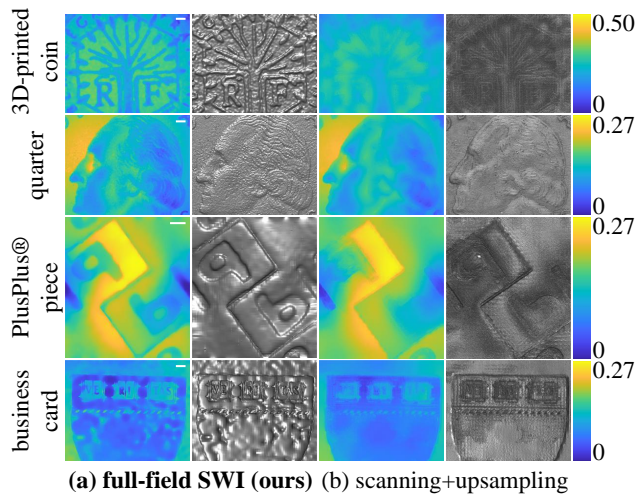


Figure 9. **Comparison with upsampled scanning SWI.** We emulate scanning SWI by downsampling our swept-angle SWI depth. We then bilaterally upsample it to the original resolution.

mitigate this bottleneck using a faster translation stage (e.g., fast microscopy stages). Alternatively, we can eliminate this bottleneck by using phase modulators and multiple mirrors, to perform the shifts without mechanical motion. We leave the development of such a prototype as future work.

Conclusion We presented a technique for fast depth sensing at micron-scale lateral and axial resolutions. Our technique, swept-angle synthetic wavelength interferometry, combines the complementary advantages of full-field interferometry (speed, pixel-level lateral resolution) and scanning interferometry (robustness to aberrations and indirect illumination). We demonstrated its advantages by scanning a variety of scenes with fine geometric features and strong subsurface scattering. We expect that our results will facilitate applications of swept-angle SWI in areas such as biomedical imaging, and industrial fabrication and inspection (Figure 1).

References

- [1] Supreeth Achar, Joseph R Bartels, William L Whittaker, Kiriakos N Kutulakos, and Srinivasa G Narasimhan. Epipolar time-of-flight imaging. *ACM TOG*, 2017. 3
- [2] Brian Aull. 3d imaging with geiger-mode avalanche photodiodes. *Opt. Photon. News*, 2005. 2
- [3] Seung-Hwan Baek, Noah Walsh, Ilya Chugunov, Zheng Shi, and Felix Heide. Centimeter-wave free-space neural time-of-flight imaging. *ACM Transactions on Graphics (TOG)*, 2022. 2, 7
- [4] Stephen T. Barnard and William B. Thompson. Disparity analysis of images. *IEEE TPAMI*, 1980. 2
- [5] Ayush Bhandari, Achuta Kadambi, Refael Whyte, Christopher Barsi, Micha Feigin, Adrian Dorrington, and Ramesh Raskar. Resolving multipath interference in time-of-flight imaging via modulation frequency diversity and sparse regularization. *Optics Letters*, 2014. 3
- [6] Tongbo Chen, Hans-Peter Seidel, and Hendrik P. A. Lensch. Modulated phase-shifting for 3d scanning. *IEEE/CVF CVPR*, 2008. 2
- [7] Yeou-Yen Cheng and James C. Wyant. Two-wavelength phase shifting interferometry. *Applied Optics*, 1984. 3, 7
- [8] Yeou-Yen Cheng and James C. Wyant. Multiple-wavelength phase-shifting interferometry. *Applied Optics*, 1985. 3, 7
- [9] Peter de Groot. *Phase Shifting Interferometry*. 2011. 2, 6
- [10] Peter de Groot and John McGarvey. Chirped synthetic-wavelength interferometry. *Optics Letters*, 1992. 3
- [11] David Droschel, Dirk Holz, and Sven Behnke. Multi-frequency phase unwrapping for time-of-flight cameras. *IEEE/RSJ IROS*, 2010. 7
- [12] Elmar Eisemann and Frédo Durand. Flash photography enhancement via intrinsic relighting. *ACM transactions on graphics (TOG)*, 2004. 6
- [13] Adolf F Fercher, Wolfgang Drexler, Christoph K Hitzenberger, and Theo Lasser. Optical coherence tomography-principles and applications. *Reports on progress in physics*, 2003. 3
- [14] Adolf F. Fercher, H Z. Hu, and U. Vry. Rough surface interferometry with a two-wavelength heterodyne speckle interferometer. *Applied Optics*, 1985. 3
- [15] Richard Ferriere, Johann Cussey, and John M. Dudley. Time-of-flight range detection using low-frequency intensity modulation of a cw laser diode: application to fiber length measurement. *Optical Engineering*, 2008. 2
- [16] Angel Flores, Craig Robin, Ann Lanari, and Iyad Dajani. Pseudo-random binary sequence phase modulation for narrow linewidth, kilowatt, monolithic fiber amplifiers. *Optics Express*, 2014. 2
- [17] Daniel Freedman, Eyal Krupka, Yoni Smolin, Ido Leichter, and Mirko Schmidt. Sra: Fast removal of general multipath for tof sensors, 2014. 3
- [18] Stefan Fuchs. Multipath interference compensation in time-of-flight camera images. *ICPR*, 2010. 3
- [19] Genevieve Garipey, Nikola Krstajić, Robert Henderson, Chunyong Li, Robert R Thomson, Gerald S Buller, Barmak Heshmat, Ramesh Raskar, Jonathan Leach, and Daniele Facio. Single-photon sensitive light-in-flight imaging. *Nature Comm.*, 2015. 2
- [20] Ioannis Gkioulekas, Anat Levin, Frédo Durand, and Todd Zickler. Micron-scale light transport decomposition using interferometry. *ACM TOG*, 2015. 3, 5, 6, 15, 17
- [21] P. Grossmann. Depth from focus. *PRL*, 1987. 2
- [22] Anant Gupta, Atul Ingle, and Mohit Gupta. Asynchronous single-photon 3d imaging. In *ICCV*, 2019. 2
- [23] Anant Gupta, Atul Ingle, Andreas Velten, and Mohit Gupta. Photon-flooded single-photon 3d cameras. *IEEE/CVF CVPR*, 2019. 2
- [24] Mohit Gupta, Amit Agrawal, Ashok Veeraraghavan, and Srinivasa G Narasimhan. Structured light 3d scanning in the presence of global illumination. *IEEE/CVF CVPR*, 2011. 2
- [25] Mohit Gupta, Shree K Nayar, Matthias B Hullin, and Jaime Martin. Phasor imaging: A generalization of correlation-based time-of-flight imaging. *ACM TOG*, 2015. 3, 7
- [26] Mohit Gupta, Andreas Velten, Shree K. Nayar, and Eric Breitenbach. What are optimal coding functions for time-of-flight imaging? *ACM TOG*, 2018. 2
- [27] Felipe Gutierrez-Barragan, Syed Azer Reza, Andreas Velten, and Mohit Gupta. Practical coding function design for time-of-flight imaging. *IEEE/CVF CVPR*, 2019. 2
- [28] Yudeog Han, Joon-Young Lee, and In So Kweon. High quality shape from a single rgb-d image under uncalibrated natural illumination. *IEEE ICCV*, 2013. 2
- [29] Parameswaran Hariharan. *Optical interferometry*. Elsevier, 2003. 2
- [30] Richard Hartley and Andrew Zisserman. *Multiple View Geometry in Computer Vision*. 2004. 2
- [31] Caner Hazirbas, Sebastian Georg Soyer, Maximilian Christian Staab, Laura Leal-Taixé, and Daniel Cremers. Deep depth from focus, 2018. 2
- [32] Felix Heide, Steven Diamond, David B. Lindell, and Gordon Wetzstein. Sub-picosecond photon-efficient 3d imaging using single-photon sensors. *Scientific Reports*, 2018. 2
- [33] Felix Heide, Matthias B Hullin, James Gregson, and Wolfgang Heidrich. Low-budget transient imaging using photonic mixer devices. *ACM TOG*, 2013. 2
- [34] Berthold Klaus Paul Horn. Shape from shading: A method for obtaining the shape of a smooth opaque object from one view. Technical report, 1970. 2
- [35] David Huang, Eric A Swanson, Charles P Lin, Joel S Schuman, William G Stinson, Warren Chang, Michael R Hee, Thomas Flotte, Kenton Gregory, Carmen A Puliafito, and James G Fujimoto. Optical coherence tomography. *Science*, 1991. 3
- [36] David Jimenez, Daniel Pizarro, Manuel Mazoa, and Sira Palazuelos. Modeling and correction of multipath interference in time of flight cameras. *Image and Vision Computing*, 2014. 3
- [37] Jon L. Johnson, Timothy D. Dorney, and Daniel M. Mittleman. Enhanced depth resolution in terahertz imaging using phase-shift interferometry. *Applied Physics Letters*, 2001. 2
- [38] Achuta Kadambi, Refael Whyte, Ayush Bhandari, Lee Streeter, Christopher Barsi, Adrian Dorrington, and Ramesh

- Raskar. Coded Time of Flight Cameras: Sparse Deconvolution to Address Multipath Interference and Recover Time Profiles. *ACM TOG*, 2013. 3
- [39] Ahmed Kirmani, Dheera Venkatraman, Dongeek Shin, Andrea Colaço, Franco N. C. Wong, Jeffrey H. Shapiro, and Vivek K Goyal. First-photon imaging. *Science*, 2014. 2
- [40] Johannes Kopf, Michael F. Cohen, Dani Lischinski, and Matt Uyttendaele. Joint bilateral upsampling. *ACM Trans. Graph.*, 26(3):96–es, jul 2007. 7
- [41] Alankar Kotwal, Anat Levin, and Ioannis Gkioulekas. Interferometric transmission probing with coded mutual intensity. *ACM TOG*, 2020. 3, 6, 15
- [42] Guanming Lai and Toyohiko Yatagai. Generalized phase-shifting interferometry. *JOSA A*, 1991. 6
- [43] Robert Lange and Peter Seitz. Solid-state time-of-flight range camera. *IEEE JQE*, 2001. 2
- [44] Robert Lange, Peter Seitz, Alice Biber, and Stefan Lauxtermann. Demodulation pixels in ccd and cmos technologies. *SPIE*, 2000. 2
- [45] Fengqiang Li, Florian Willomitzer, Prasanna Rangarajan, Mohit Gupta, Andreas Velten, and Oliver Cossairt. Sh-tof: Micro resolution time-of-flight imaging with superheterodyne interferometry. *IEEE ICCP*, 2018. 3
- [46] Fengqiang Li, Joshua Yablon, Andreas Velten, Mohit Gupta, and Oliver Cossairt. High-depth-resolution range imaging with multiple-wavelength superheterodyne interferometry using 1550-nm lasers. *Applied Optics*, 2017. 3
- [47] David B Lindell, Matthew O’Toole, and Gordon Wetzstein. Single-photon 3d imaging with deep sensor fusion. *ACM TOG*, 2018. 2
- [48] Xiaomeng Liu, Kristofer Henderson, Joshua Rego, Suren Jayasuriya, and Sanjeev Koppal. Dense lissajous sampling and interpolation for dynamic light-transport. *Optics Express*, 2021. 15
- [49] Julio Marco, Quercus Hernandez, Adolfo Muñoz, Yue Dong, Adrian Jarabo, Min H. Kim, Xin Tong, and Diego Gutierrez. Deeptof: Off-the-shelf real-time correction of multipath interference in time-of-flight imaging. *ACM TOG*, 2017. 3
- [50] Inc. Mirrorcle Technologies. Mirrorcle mems technical overview, 2022. https://www.mirrorcletech.com/pdf/Mirrorcle_MEMS_Mirrors_-_Technical_Overview.pdf. 13
- [51] Nikhil Naik, Achuta Kadambi, Christoph Rhemann, Shahram Izadi, Ramesh Raskar, and Sing Bing Kang. A light transport model for mitigating multipath interference in time-of-flight sensors. *IEEE/CVF CVPR*, 2015. 3
- [52] Lazaros Nalpantidis, Georgios Sirakoulis, and Antonios Gasteratos. Review of stereo vision algorithms: From software to hardware. *Int. J. Optomechatronics*, 2008. 2
- [53] Shree Nayar, Gurunandan Krishnan, Michael Grossberg, and Ramesh Raskar. Fast separation of direct and global components of a scene using high frequency illumination. *ACM TOG*, 2006. 3
- [54] Cristiano Niclass, Alexis Rochas, Pierre. Besse, and Edoardo Charbon. Design and characterization of a cmos 3-d image sensor based on single photon avalanche diodes. *IEEE JSSC*, 2005. 2
- [55] Matthew O’Toole, Supreeth Achar, Srinivasa G Narasimhan, and Kiriakos N Kutulakos. Homogeneous codes for energy-efficient illumination and imaging. *ACM TOG*, 2015. 3
- [56] Matthew O’Toole, Felix Heide, David B Lindell, Kai Zang, Steven Diamond, and Gordon Wetzstein. Reconstructing transient images from single-photon sensors. *IEEE/CVF CVPR*, 2017. 2
- [57] Matthew O’Toole, Felix Heide, Lei Xiao, Matthias B Hullin, Wolfgang Heidrich, and Kiriakos N Kutulakos. Temporal Frequency Probing for 5D Transient Analysis of Global Light Transport. *ACM TOG*, 2014. 3
- [58] Matthew O’Toole, John Mather, and Kiriakos N. Kutulakos. 3d shape and indirect appearance by structured light transport. *IEEE TPAMI*, 2016. 2, 3
- [59] Matthew O’Toole, Ramesh Raskar, and Kiriakos N Kutulakos. Primal-dual Coding to Probe Light Transport. *ACM TOG*, 2012. 3
- [60] Andrew Payne, A Dorrington, and Michael Cree. Illumination waveform optimization for time-of-flight range imaging cameras. *SPIE*, 2011. 2
- [61] Georg Petschnigg, Richard Szeliski, Maneesh Agrawala, Michael Cohen, Hugues Hoppe, and Kentaro Toyama. Digital photography with flash and no-flash image pairs. *ACM transactions on graphics (TOG)*, 2004. 6
- [62] Dario Piatti, Fabio Remondino, and David Stoppa. *State-of-the-Art of TOF Range-Imaging Sensors*. 2013. 2
- [63] Dikpal Reddy, Ravi Ramamoorthi, and Brian Curless. Frequency-space Decomposition and Acquisition of Light Transport Under Spatially Varying Illumination. *ECCV*, 2012. 3
- [64] Alexis Rochas, Michael Gosch, Alexandre Serov, Pierre Besse, Rade S. Popovic, T. Lasser, and Rudolph Rigler. First fully integrated 2-d array of single-photon detectors in standard cmos technology. *IEEE PTL*, 2003. 2
- [65] Daniel Scharstein and Richard Szeliski. High-accuracy stereo depth maps using structured light. *IEEE/CVF CVPR*, 2003. 2
- [66] Rudolf Schwarte, Zhanping Xu, Horst-Guenther Heinol, Joachim Olk, Ruediger Klein, Bernd Buxbaum, Helmut Fischer, and Juergen Schulte. New electro-optical mixing and correlating sensor: facilities and applications of the photonic mixer device (PMD). In *Sensors, Sensor Systems, and Sensor Data Processing*, 1997. 2
- [67] Pitchaya Sitthi-Amorn, Javier E Ramos, Yuwang Wangy, Joyce Kwan, Justin Lan, Wenshou Wang, and Wojciech Matusik. Multifab: a machine vision assisted platform for multi-material 3d printing. *Acm Transactions on Graphics (Tog)*, 2015. 2
- [68] Shuo Chen Su, Felix Heide, Gordon Wetzstein, and Wolfgang Heidrich. Deep end-to-end time-of-flight imaging. *CVPR*, 2018. 3
- [69] Murali Subbarao and Gopal Surya. Depth from defocus: A spatial domain approach. *IJCV*, 1994. 2
- [70] Orazio Svelto. *Principles of Lasers*. 2010. 12, 13
- [71] Andreas Velten, Thomas Willwacher, Otkrist Gupta, Ashok Veeraraghavan, Mounqi G. Bawendi, and Ramesh Raskar. Recovering three-dimensional shape around a corner using ultrafast time-of-flight imaging. *Nature Comm.*, 2012. 2

- [72] Federica Villa, Rudi Lussana, Danilo Bronzi, Simone Tisa, Alberto Tosi, Franco Zappa, Alberto Dalla Mora, Davide Contini, Daniel Durini, Sasha Weyers, and Werner Brockherde. Cmos imager with 1024 spads and tdc's for single-photon timing and 3-d time-of-flight. *IEEE JSTQE*, 2014. 2
- [73] Peng Xiao, Mathias Fink, and A Claude Boccara. Full-field spatially incoherent illumination interferometry: a spatial resolution almost insensitive to aberrations. *Optics letters*, 2016. 5

A. Proofs

Proof of Equation (2). Synthetic wavelength interferometry uses illumination comprising two distinct, but narrowly-separated, incoherent lasers. We denote the wavelengths of these lasers as λ and $\lambda/1+\epsilon$, corresponding to wavenumbers $\kappa \equiv 2\pi/\lambda$ and $(1+\epsilon)\kappa$, respectively. In full-field SWI, the outputs of these two lasers are placed in the focal plane of a lens that forms a collimated beam. When the output of the laser with wavelength λ is placed on the optical axis of the interferometer, it results in a wavefront propagating parallel to the optical axis. Then, the wave field propagating towards the beamsplitter is

$$\mathbf{u}_i^\kappa(x, z) = \exp(-i\kappa z). \quad (12)$$

When the scene point at x is placed at a distance $d(x)$ from the beamsplitter, the illumination travels $2d(x)$ in the scene arm, accounting for the propagation to the scene and back. Then, the field due to the scene at the sensor pixel x is

$$\mathbf{u}_s^\kappa(x) = \exp(-i\kappa(2d(x) + l_0)), \quad (13)$$

where l_0 incorporates the travel distance from the lens to the beamsplitter and the beamsplitter to the sensor. Similarly, when the reference arm is placed at a distance l from the beamsplitter, the field due to the reference arm at the sensor pixel x is

$$\mathbf{u}_r^\kappa(x, l) = \exp(-i\kappa(2l + l_0)). \quad (14)$$

Then, the correlation $\mathcal{C}^\kappa(x, l)$ for the wavelength λ equals

$$\begin{aligned} \mathcal{C}^\kappa(x, l) &= \mathbf{u}_s(x)\mathbf{u}_r^*(x, l) \\ &= \exp(-2i\kappa(d(x) + l_0)) \exp(i\kappa(l + l_0)) \\ &= \exp(-2i\kappa(d(x) - l)). \end{aligned} \quad (15)$$

Since the two lasers are incoherent with each other, there are no cross-correlations between the fields. Therefore, $\mathcal{C}(x, l)$ for both lasers together is given by the *incoherent* sum of their correlations:

$$\begin{aligned} \mathcal{C}(x, l) &= \mathcal{C}^\kappa(x, l) + \mathcal{C}^{(1+\epsilon)\kappa}(x, l) \\ &= \exp(-2i\kappa(d(x) - l)) \\ &\quad + \exp(-2i\kappa(1+\epsilon)(d(x) - l)) \\ &= \exp(-2i\kappa(d(x) - l)) \\ &\quad [1 + \exp(-2i\kappa\epsilon(d(x) - l))]. \end{aligned} \quad (16)$$

thus proving Equation (2) from the main paper.

Four-bucket algorithm. Here, we detail depth reconstruction using the $\{4, 4\}$ -shift phase retrieval algorithm. Equation (11) from the main paper gives us the capability to estimate only the magnitude $|\mathcal{E}(x, l)|$ of the envelope and not the sign. However, we can rewrite the *squared magnitude* of the envelope as a sinusoid:

$$|\mathcal{E}(x, l)|^2 = \sin^2(\kappa\epsilon(d(x) - l)) \quad (17)$$

$$= \frac{1 - \cos(2\kappa\epsilon(d(x) - l))}{2}. \quad (18)$$

The period of this sinusoid is half the synthetic wavelength

λ_s . Taking measurements at $l_n = l + n\lambda_s/2N$ for $N \in \{0, \dots, N-1\}$, we can estimate depth as

$$d(x) = l + \frac{1}{2\kappa\epsilon} \arctan \left[\frac{\sum_{n=0}^{N-1} |\mathcal{E}(x, l_n)|^2 \sin(2\pi n/N)}{\sum_{n=0}^{N-1} |\mathcal{E}(x, l_n)|^2 \cos(2\pi n/N)} \right]. \quad (19)$$

B. Scanning versus full-field comparison

Scan points for equal-time acquisition. In Figure 9 of the main paper, we show depth reconstructions with full-field swept-angle SWI and upsampled point scanning SWI for the $\{4, 4\}$ -shift algorithm. To emulate point scanning, we downsampled the SWI depth by a factor of 35 in each dimension, and claimed that corresponds to an equal-time comparison for a 30 kHz MEMS scanner. Here, we will detail this calculation.

Our swept-angle SWI system, for scenes with very low reflectivity, performs depth sensing at 1 Hz. In the equivalent time of 1 s, the scanner has to perform 16 passes over the scene to take the 16 measurements required for the $\{4, 4\}$ -shift algorithm. This makes the maximum number of points that the scanner can measure in two dimensions $30000/16 = 1875$. In one dimension, this translates to $\sqrt{1875} \approx 43$ points. Our images have the approximate dimension 1600×1300 . Distributing these points equally along the larger dimension yields a downsampling factor of $1600/43 \approx 35$.

We note that this calculation is already favorable for the scanning system, for two reasons. First, the typical scan rate will be lower than the nominal scan rate of 30 kHz, because of the need to scan a larger field of view, or the inability to drive both axes at resonant mode. Second, for scenes with high reflectivity (e.g., metallic scenes), our setup operates at 10 Hz, and thus the number of scanned points for the scanning system should be $10\times$ fewer.

Challenges for achieving micrometer lateral resolutions with scanning systems. We discuss in more detail some of the challenges associated with achieving micrometer lateral resolutions using a scanning system. Doing so requires: (i) a laser beam that can be collimated or focused at a few micrometers; (ii) a MEMS mirror capable of scanning at high-enough angular resolution to translate the laser beam a few microns on the scene surface; and (iii) acquisition time long enough to scan a megapixel-size grid on the scene. Each of these requirements is difficult to achieve:

- (i) The diameter of a Gaussian laser beam is inversely proportional to its divergence [70, Chapter 4]. The smaller the beam diameter, the larger the divergence. At 780 nm, a laser beam with a diameter of $1 \mu\text{m}$ grows in diameter by 10% every 2 m. Therefore, maintaining collimation diameter of $1 \mu\text{m}$ is challenging except for very small working distances.

As an alternative to using a thin, collimated laser beams, we can use a beam that is focused at each point on the scene. Contrary to micron-scale beam waists, it is possible to focus single-model lasers to pixel-size spot sizes [70, Chapter 9] However, focusing the laser beam onto the scanned scene points sharply decreases the depth of field of the imaging system: Whereas, in the case of a collimated beam, the depth of field is limited by the divergence of the collimated beam, in the case of a focused beam, it is limited by the quadratic phase profile of the focused spot. Effectively, to use this focused setup, we need another axial scan to ensure that the scanned post is within the depth of field, which only adds to acquisition time.

- (ii) Top-of-the-line scanning micromirrors typically have angular scanning resolutions of $10\ \mu\text{rad}$ [50]. The maximum working distance such that this would correspond to micrometer lateral resolution is 10 cm.
- (iii) The scanning micromirror needs to be run in “point-to-point scanning mode” [50], where the micromirror stops at every desired position. The best settling times for step mirror deflections are around $100\ \mu\text{s}$ [50]. Using these numbers, for a megapixel image, the micromirror rotations require acquisition time around 100 s.

A swept-angle full-field interferometer does not need to perform lateral scanning. Instead, it accomplishes direct-only (i.e., coaxial) imaging by scanning an area in the focal plane of the collimating lens, an operation that can be done in the resonant mode of a MEMS mirror within exposure.

C. Additional experiments

Trade-off between acquisition time and depth quality. The theoretical minimum number of measurements needed to reconstruct depth using SWI is 9 ($M = N = 3$). However, increasing M and N makes the depth reconstruction robust to measurement and speckle noise, yielding higher quality depth. There is, therefore, a trade-off between number of measurements $M \cdot N$ and depth quality.

Besides number of measurements, another factor contributing to acquisition time is the MEMS mirror scan we perform to create swept-angle illumination. If we decrease acquisition time, giving the mirror lesser time to complete one full scan of the source in the focal plane of the collimating lens, the spatial density of scanned points on the simulated emission area decreases. This reduces the effectivity of rejecting indirect light, and therefore reduces depth quality. This, again, creates a trade-off between acquisition time and depth quality.

In Figure 10, we demonstrate the effect of both these factors on depth quality. On the horizontal dimension, we

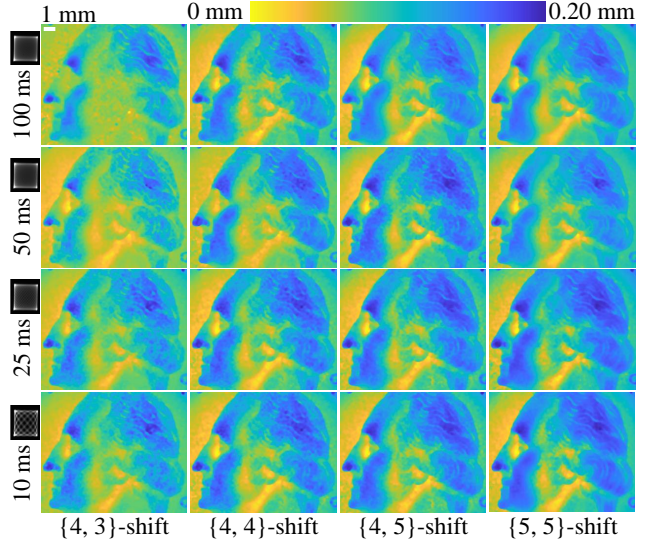


Figure 10. **Depth quality and acquisition time.** We show qualitatively the effects of per-image acquisition time (dictated by the period of the MEMS mirror scan) and the number of images acquired $M \cdot N$ on the quality of the reconstructed depth. The pattern in the black box next to per-image times is the scanned emission area in the focal plane of the illumination lens.

use different $\{M, N\}$ -shift phase retrieval algorithms, and on the vertical dimension, we use different per-image acquisition times as dictated by the scan time of the MEMS mirror. We observe that using higher M and N allows us to reduce the per-image acquisition time by requiring a lower scanned source density for equal visual depth quality. In particular, the 100 ms scan with the $\{4, 5\}$ -shift algorithm performs as well as the 10 ms scan with the $\{5, 5\}$ -shift algorithm, allowing us to reduce total acquisition time from 2 s to 250 ms.

Tunable depth range. The use of two wavelengths in synthetic wavelength interferometry makes it possible to control the unambiguous depth range: By decreasing the separation $\kappa\epsilon$ between the two laser wavelengths, we increase the unambiguous depth range, at the cost of decreasing depth resolution. In particular, picometer separations in wavelengths result in synthetic wavelengths of centimeters. We use this to scan the *macroscopic* scenes in Figure 11, which have a depth range of approximately 1 cm. In all three scenes, the use of swept-angle illumination greatly improves reconstruction quality, by mitigating the effects of the significant subsurface scattering present in all scenes.

We note that achieving picometer-scale wavelength separation requires using current-based tuning of the wavelength of the DBR lasers in our setup. The DBR lasers have a linear response of wavelength to current near their operating point, and tuning current by 50 mA gives picometer-scale wavelength separations.

Robustness to ambient light. In Figure 12, we demonstrate the robustness of our method to ambient light on the

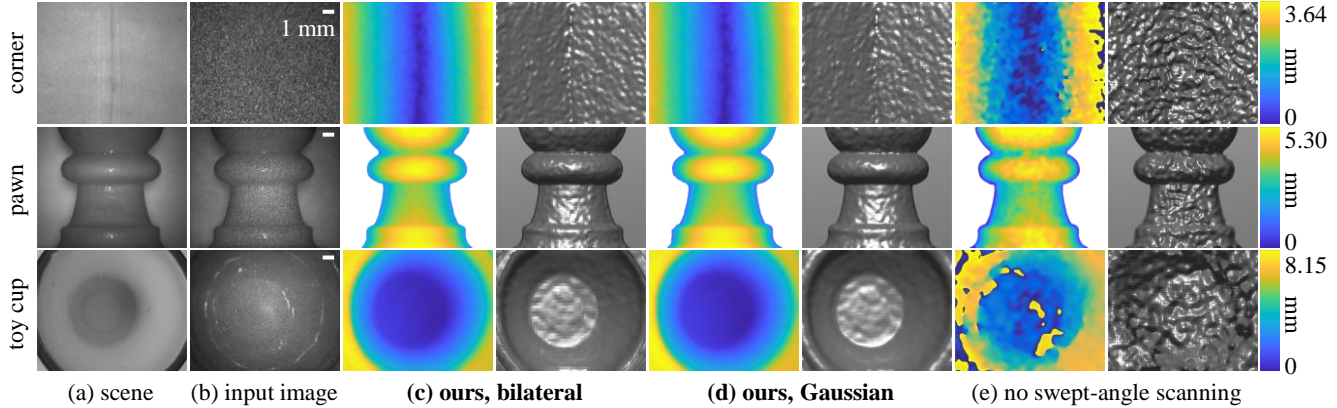


Figure 11. **Depth reconstruction.** Depth maps (left) and surface renderings (right) acquired using full-field SWI with: (c) swept-angle scanning and bilateral filtering; (d) swept-angle scanning and Gaussian filtering; (e) no swept-angle scanning and with Gaussian filtering.

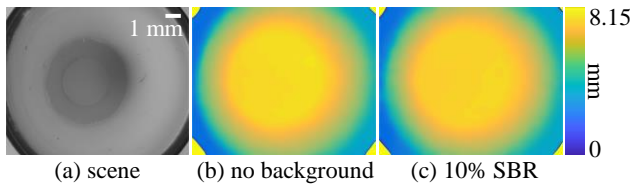


Figure 12. **Robustness to ambient light.** In (c), we shine external light on the sample so that the signal-to-background ratio (SBR) our laser illumination to ambient noise is 0.1. This greatly decreases the contrast of the interference speckle pattern. Despite this, there is little degradation in the quality of our recovered depth.

toy cup scene from Figure 11. We shine a spotlight on the scene such that the signal-to-background ratio (SBR) of the laser illumination to ambient light is 0.1. Ambient light adds to the intensity measurement at the camera, but not to interference, thus reducing interference contrast and potentially degrading the depth reconstruction. However, we see that at this SBR, the depth recovered from the toy cup scene (Figure 12(d)) is very close to the depth recovered without ambient light (Figure 12(c)). In addition, we can further reject ambient light by using an ultra-narrow spectral filter centered at the average illumination wavelength. This is possible because SWI uses illumination comprising two very narrowly-separated wavelengths.

Depth accuracy. We show here the data we captured to assess our depth accuracy in Table 1 of the main paper. Figure 13 plots, on top, the estimated SWI depth relative to the ground truth depth provided by the scene translation stage. Figure 13(a) is captured with the swept-angle mechanism, whereas Figure 13(b) is captured with the mechanism off. Comparing the two figures, we see that the measured depth correlates with the ground truth depth a lot stronger when we use swept-angle illumination versus when we do not.

Figure 13(c) and Figure 13(d) respectively show the same experiment performed at a *macroscopic* synthetic wavelength of 16 mm, the same as in Figure 11. These measurements also depict that swept-angle scanning is critical

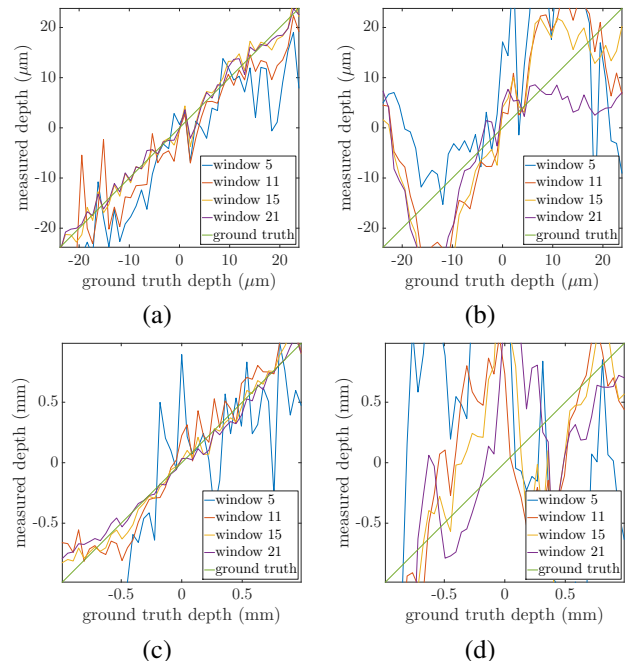


Figure 13. **Testing the depth resolution of our method.** We place the chocolate scene from Figure 14 at different distances from the camera using a translation stage and capture measurements using our method at each position. We do this under four conditions: (a) microscopic synthetic wavelength with swept-angle, (b) microscopic synthetic wavelength without swept-angle, (c) macroscopic synthetic wavelength with swept-angle, and (d) macroscopic synthetic wavelength without swept-angle. In each case, we plot the depth measured by our method against the ground truth position of the scene provided by the translation stage. The window parameter in the plots is the size of the Gaussian blur kernel.

for micron-scale depth sensing. We show the error numbers from this experiment, similar to Table 1 in the main paper, in Table 3. With a kernel width of 150 μm , we are able to achieve depth accuracies of 50 μm .

Comparison with full-field OCT As mentioned in the main paper, depth sensing with full-field spatially-

Table 3. **Depth accuracy with synthetic wavelength** 16 mm. MedAE is the median absolute error between ground truth and estimated depth. Kernel width is the lateral size of the speckle blur filter. All quantities are in μm .

kernel width	with swept-angle		w/o swept-angle	
	RMSE	MedAE	RMSE	MedAE
7	471.4	300.3	1267.2	1351.0
15	167.1	120.5	577.9	501.9
21	78.7	50.9	609.5	412.2
30	81.7	49.6	605.7	334.4

incoherent OCT achieves unambiguous depth ranges up to centimeters at micrometer axial resolutions. Here, we demonstrate that swept-angle SWI approximates the reconstruction quality of full-field OCT, while being $50\times$ faster. Figures 14 and 15 compare the performance of swept-angle SWI with full-field OCT implemented as in Gkioulekas et al. [20]. We also depict differences between swept-angle SWI and OCT depth reconstructions.

We use time-domain OCT to capture these scenes. Time-domain OCT requires a reference mirror scan spanning the depth range of the scene spaced at equal intervals of the desired depth resolution. For $500\ \mu\text{m}$ depth range and $1\ \mu\text{m}$ axial resolution, the number of measurements OCT requires that is 500. By contrast, SWI can capture depth with comparable quality in $M \cdot N$ measurements. For the comparison in Figure 14, we use $4 \cdot 4 = 16$ measurements, which makes SWI $30\times$ faster than OCT at comparable reconstruction quality. As we show in Figure 10, we can achieve similar reconstruction quality using SWI with $3 \cdot 3 = 9$ measurements, making SWI $50\times$ faster than OCT.

D. Acquisition setup

We discuss here the engineering details of the setup implementing swept-angle synthetic wavelength interferometry. The schematic and a picture of the setup are shown in Figure 5(c) of the main paper. We use similar components as in the setup of Kotwal et al. [41], and replicate the implementation details below for completeness.

Light source. We use near-infrared single frequency tunable laser diodes from Thorlabs (DBR780PN, 780 nm, 45 mW, 1 MHz linewidth). These laser diodes are tunable in wavelength by adjusting either operating current or temperature of the diode. To create small wavelength separations (of the order of 0.01 nm), we modulate the operating current of one laser diode with a square waveform, thus create two time-multiplexed wavelengths. To create larger separations (of the order of 1 nm), we use two different laser diodes selected at the appropriate central wavelengths. This is possible because the central wavelengths of separately manufactured laser diodes vary in a $\pm 2\ \text{nm}$ region around 780 nm. We found that for accurate depth recovery, it is important for the light sources to be monochromatic (single

longitudinal mode), stable in wavelength and power, and accurately tunable. We experimented with multiple alternatives and encountered problems with either stability, tunability or monochromaticity. We found the DBR lasers from Thorlabs optimal in all these aspects.

Calibrating the synthetic wavelength. The synthetic wavelength resulting from this illumination is very sensitive to the separation between the two wavelengths, especially at microscopic scales. Therefore, after selecting a pair of lasers or current levels for an approximate synthetic wavelength, it is necessary to estimate the actual synthetic wavelength accurately. To do this, we measure the envelope sinusoid for a planar diffuser scene at a dense collection of reference arm positions. We then fit a sinusoid to these measured magnitudes and use the fit wavelength as the synthetic wavelength.

Mechanism for swept-angle scanning. We use two fast-rotating mirrors to scan the laser beam in $1^\circ \times 1^\circ$ angular pattern at slightly separated kHz frequencies, as shown by Kotwal et al. [41] and Liu et al. [48]. A 35 mm Nikon prime lens then maps beam orientation to spatial coordinates behind the illumination lens, creating the light source for swept-angle illumination. The created light source is a dense Lissajous curve that approximates a square. Figure 16 shows an example light source scanned in this fashion. In practice, we use a much denser light source, but show the coarse one in the inset only to make the Lissajous pattern visible.

Illumination lens. We place the above light source in the focal plane of a 200 mm Nikon prime lens to generate the swept-angle illumination. Photographic lenses perform superior to AR-coated achromatic doublets in terms of spherical and chromatic aberration, therefore resulting in significantly lesser distortion in the generated wavefront.

Interreflections. Interreflections are problematic for us because our illumination is temporally coherent. Interreflections introduce multiple light paths that interfere with each other to create strong spurious fringes. Such fringes suppress the contrast of our speckle signal. The optics we use are coated with anti-reflective films designed for our laser wavelengths to reduce interreflections. We also deliberately misalign our optics with sub-degree rotations from the ideal alignment to avoid strong interreflections.

Beamsplitter. We use a thin 50:50 plate beamsplitter, since pellicle and cube beamsplitters cause strong fringes. As above, we deliberately misalign the beamsplitter to avoid interreflections.

Mirrors. We use high-quality mirrors of guaranteed $\lambda/4$



Figure 16. Lissajous curve scanned in the focal plane of the collimating lens

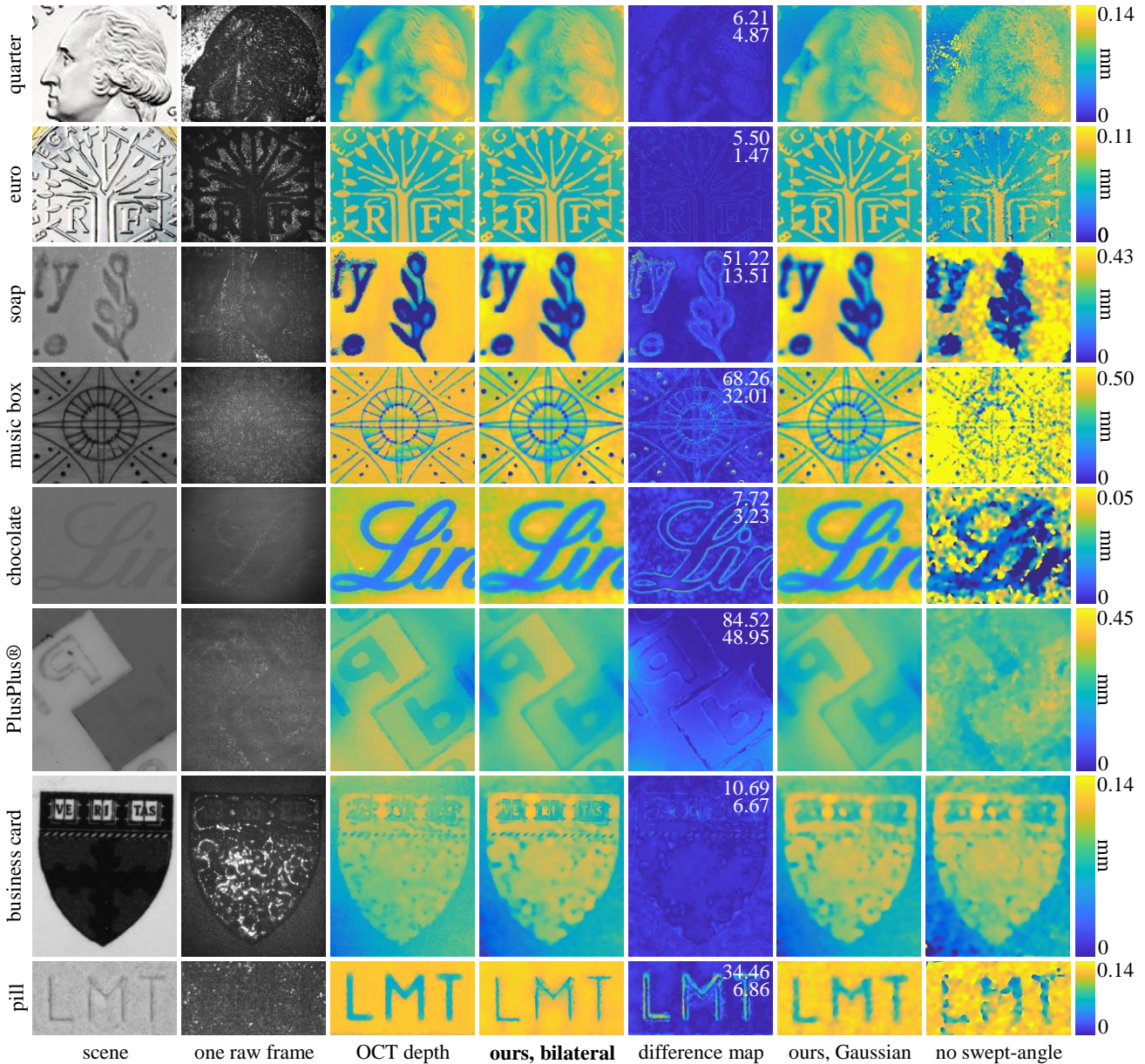


Figure 14. **Comparing swept-angle SWI and full-field OCT in microscopic scenes.** The difference maps show the absolute difference between recovered OCT and swept-angle SWI depths, and report the root-mean-square (top) and mean absolute (bottom) differences between the two. The OCT depths are captured at a resolution comparable to swept-angle SWI.

flatness to ensure a uniform phase reference throughout the field of view of the camera.

Translation stage. We use an ultra-precision motorized linear translation stage from Newport with a positioning accuracy of up to 10 nm and minimum incremental motion of 1 nm. For high-resolution depth recovery, it is important that the mirror positions images are captured at be accurate at sub-optical wavelength scales. In addition, it is important that the translation stage guarantee low-positioning-noise operation.

Camera lens. Our scenes are sized at the order of 1 inch. Therefore, we benefit from a lens that achieves high magnifications (1:1 reproduction ratio). This also allows for better contrast due to lower averaging of speckle (interference signal is convolved with the pixel box when captured with the camera). We use a 180 mm Canon prime macro lens in front of the camera.

Camera. We use a machine vision camera from Allied Vision with a high-sensitivity CCD sensor of 8 MP resolution, and pixel size 3.5 μm . A sensor with a small pixel pitch

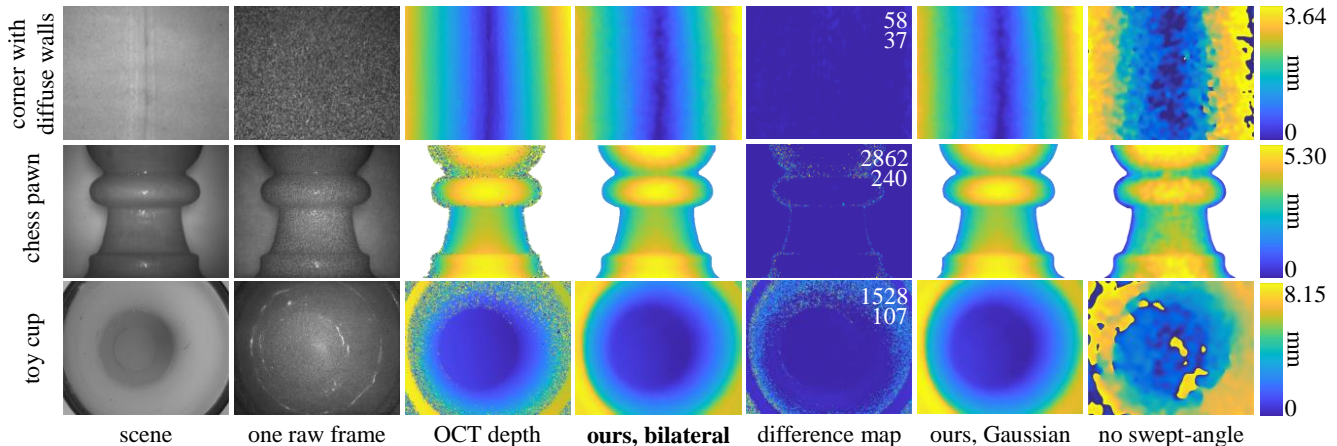


Figure 15. **Comparing swept-angle SWI and full-field OCT in macroscopic scenes.** The difference maps show the absolute difference between recovered OCT and swept-angle SWI depths, and report the root-mean-square (top) and mean absolute (bottom) differences between the two. The OCT depths are captured at a resolution comparable to swept-angle SWI.

Table 4. List of major components used in the optical setup of Figure 5(c) of the main paper.

description	quantity	model name	company
single-frequency lasers, 780 nm CWL, 45 mW power	2	DBR780PN	Thorlabs
benchtop laser diode current controller, ± 500 mA HV	2	LDC205C	Thorlabs
benchtop temperature controller, ± 2 A / 12 WW	2	TED200C	Thorlabs
1 \times 2 polarization-maintaining fiber coupler, 780 \pm 15 nm	1	PN780R5A1	Thorlabs
reflective FC/APC fiber collimator	1	RC04APC-P01	Thorlabs
2 \times beam expander	1	GBE02-B	Thorlabs
2-axis galvanometer mirror set	1	GVS202	Thorlabs
function generator	2	SDG1025	Siglent
35 mm compound lens	1	AF Micro Nikkor 35mm 1:4 D IF-ED	Nikon
200 mm compound lens	1	AF Micro Nikkor 200mm 1:4 D IF-ED	Nikon
25 mm \times 36 mm plate beamsplitter	3	BSW10R	Thorlabs
1 inch round protected Aluminum mirror	3	ME1-G01	Thorlabs
2 inch absorptive neutral density filter kit	1	NEK01S	Thorlabs
ultra-precision linear motor stage, 16 cm travel	1	XMS160	Newport Corporation
ethernet driver for linear stage	1	XPS-Q2	Newport Corporation
780.5 \pm 1 nm OD6 ultra-narrow spectral filter	1	-	Alluxa
180 mm compound lens	1	EF 180mm f/3.5L Macro USM	Canon
8 MP CCD color camera with Birger EF mount	1	PRO-GT3400-09	Allied Vision Technologies

averages interference speckle over a smaller spatial area, therefore allowing us to resolve finer lateral detail. We use a camera with the protective glass of sensor removed. This is critical to avoid spurious interreflections caused by the protective glass.

Neutral density filters. We use absorptive neutral density filters to optimize interference contrast by making the intensities of both interferometer arms equal.

Alignment. For depth estimation accurate to micron-scales, the optical setup requires very careful alignment. To avoid as much human error as possible, we build the illumination side and the beamsplitter holder on a rigid cage system constructed with components from Thorlabs. To ensure a mean direction of light propagation that’s parallel to the optical axis of the interferometer, we tune the steering mirrors electronically by adjusting their driving waveform’s DC offset.

We then align the reference mirror and camera using the alignment technique described by Gkioulekas et al. [20].

Component list. For reproducibility, Table 4 gives a list of the important components used in our implementation.

E. Code and algorithms

We provide in Figure 17 an implementation of the {4, 4}-shift phase retrieval algorithm for recovering depth from measurements made with four subwavelength shifts and the four-bucket algorithm. The code assumes that the measurements are stored in a variable `frames` of size $H \times W \times 4 \times 4$, where H and W are the height and width of the measured images respectively, with the third dimension varying over sub-wavelength shifts and the fourth varying over four-bucket positions. The variable `scene` stores an ambient light image of the scene to serve as the guide image for

the bilateral filter, and the variable `lam` denotes the synthetic wavelength. The function `bilateralFilter` executes bilateral filtering of its first argument with its second argument as the guide image with `spatialWindow` and `intensityWindow`.

In addition, we provide in Algorithms 1 and 2 pseudocode for acquisition and reconstruction respectively using the general $\{M, N\}$ -shift phase retrieval algorithm.

Algorithm 1: Acquiring intensity measurements with swept-angle synthetic wavelength interferometry. The steps are captioned with reference to Figure 6 of the main paper.

Data: synthetic wavelength λ_s ; optical wavelength λ_o ; start position l
Result: intensity images $\mathcal{I}(x, l_n^m)$ at reference position l_n^m (defined below)
 $l_n^m = l + n\lambda_s/N + m\lambda_c/M$ for $n \in \{0, \dots, N-1\}$ and $m \in \{0, \dots, M-1\}$;
 /* Capture the intensity images in Figure 6(a) */
for bucket positions $n \in \{0, \dots, N-1\}$ **do**
 for sub-wavelength shifts $m \in \{0, \dots, M-1\}$ **do**
 move reference mirror to position l_n^m ;
 capture image $I(x, l_n^m)$;
 end
end
return $I(x, l_n^m)$

Algorithm 2: Processing intensity measurements to estimate depth in swept-angle synthetic wavelength interferometry. The steps are captioned with reference to Figure 6 of the main paper.

Data: synthetic wavelength λ_s ; optical wavelength λ_c ; start position l ; bilateral filter hyperparameters: spatial kernel size σ_s and intensity kernel size σ_i ; intensity measurements $I(x, l_n^m)$ at reference position l_n^m (defined below); scene ambient-light image $S(x)$
Result: depth map $d(x)$
 /* Initialization */
 $l_{mn} = l + n\lambda_s/N + m\lambda_c/M$ for $n \in \{0, \dots, N\}$ for $m \in \{0, \dots, M\}$;
for bucket positions $n \in \{0, \dots, M\}$ **do**
 /* Figure 6(b) */
 estimate interference-free image
 $\mathcal{I}(x, l_n) = \left(\sum_{m=0}^{M-1} I(x, l_n^m) \right) / M$;
 /* Figure 6(c) */
 estimate real parts of correlations
 $\text{Re} \{ \mathcal{C}(x, l_n^m) \} = I(x, l_n^m) - \mathcal{I}(x, l_n)$;
 estimate noisy envelope
 $\mathcal{E}^2(x, l_n) = \sum_{m=0}^{M-1} (\text{Re} \{ \mathcal{C}(x, l_n^m) \})^2 / 2M$;
 /* Figure 6(d) */
 denoise envelope using the bilateral filter
 $\mathcal{E}_{\text{bf}}^2(x, l_n) = \text{BilateralFilter}(\mathcal{E}^2(x, l_n), S(x), \sigma_s, \sigma_i)$;
end
 /* Figure 6(e) */
 estimate $d(x) = \frac{1}{2\kappa\epsilon} \arctan \left[\frac{\mathcal{E}_{\text{bf}}^2(x, l_3) - \mathcal{E}_{\text{bf}}^2(x, l_1)}{\mathcal{E}_{\text{bf}}^2(x, l_0) - \mathcal{E}_{\text{bf}}^2(x, l_2)} \right] + l$;
return $d(x)$

```

1 function depth = reconstruct(frames, lam, spatialWindow, ...
2                               intensityWindow, scene)
3 % Reconstruct depth from {4, 4}-shift swept-angle synthetic wavelength interferometry
4 % frames:           HxWx4x4 array of measurements, where the third dimension
5 %                   varies over subwavelength shifts and fourth over
6 %                   four-bucket positions
7 % lam:             synthetic wavelength
8 % spatialWindow:   spatial window for the bilateral filter
9 % intensityWindow: intensity window for the bilateral filter
10 % scene:           ambient light image of the scene
11
12 frames = im2double(frames)*4;
13 scene = im2double(scene)*4;
14
15 % Get interference-free images at each four-bucket position by averaging
16 % images captured with sub-wavelength shifts
17 interferenceFreeFrames = mean(frames, 3);
18
19 % Get interference images at each four-bucket position by subtracting
20 % interference-free images from the full images.
21 interference = frames - interferenceFreeFrames;
22
23 % Estimate the absolute values of the envelope by squaring and adding interference images
24 envelope = squeeze(sum(interference.^2, 3));
25
26 % Filter the estimated envelope with bilateral filtering using an ambient
27 % light image of the scene as the guide image
28 for position = 1:4
29     envelope(:, :, position) = bilateralFilter(envelope(:, :, position), ...
30                                               scene, spatialWindow, ...
31                                               intensityWindow);
32 end
33
34 % Apply the four-bucket phase retrieval algorithm to estimate phase
35 phase = atan2(envelope(:, :, 4) - envelope(:, :, 2), ...
36              envelope(:, :, 1) - envelope(:, :, 3));
37
38 % Convert phase to depth
39 depth = phase*lam/(2*pi);
40
41 end

```

Figure 17. Matlab code for recovering depth from {4, 4}-shift measurements